

Effect of laser power and welding speed on microstructure and mechanical properties of fibre laser-welded Inconel 617 thin sheet

Prabhat Kumar¹ · Kanhaiya Saw¹  · Uday Kumar¹ · Ratnesh Kumar¹ · Somnath Chattopadhyaya¹ · Sergej Hloch^{2,3}

Received: 26 May 2016 / Accepted: 9 February 2017 / Published online: 17 February 2017
© The Brazilian Society of Mechanical Sciences and Engineering 2017

Abstract Inconel alloy 617 was used in the present research because of its high strength and oxidation resistance in a wide range of temperatures. In this investigation, full-penetration welding of 1.5-mm-thin Inconel 617 plates in a butt configuration was carried out with a fibre laser welding machine of 400 W. The influence of different welding conditions, such as welding speed, welding power on the heat-affected zone morphology, metallurgy and mechanical properties has been discussed in detail in this study. Microstructures have been assessed by optical microscope and by field emission scanning electron microscope. On the other hand, mechanical behaviour has been analysed in terms of Vickers microhardness and compared with specimens of base materials under different welding conditions. Tensile test has been conducted on standard welded specimen and its tensile strength along with percentage elongation has been analysed and compared with base metal specimen. Surface topography at the fractured region of the specimen has also been studied. EDAX analysis has been done at different regions of the welded samples to study the chemical composition at various regions of the

welded samples. During the investigation, XRD analysis was carried out at different positions ($2\theta^\circ$) to analyse the crystallographic structure and to get the maximum intensity of the compound matrix at different positions. During the microhardness test, hardness of the base metal was found to be lower in comparison with the fusion zone due to rapid cooling.

Keywords Fibre laser welding (FLW) · Microstructure · Field emission scanning electron microscope (FESEM) · Mechanical properties · Optical microscope

1 Introduction

Inconel 617 is a nickel-based super alloy. Primarily, it is a solid solution with exceptionally good engineering properties, such as high hardness, creep resistance, oxidation resistance. It is also resistant to both reducing and oxidizing media. This alloy is widely used in aeronautic engineering, power plants, chemical industry and nuclear power industry. Components made with this alloy, such as ducting, combustion cans, transition liners, etc., are widely used both in aircraft as well as in land-based gas turbines. Due to the simultaneous presence of chromium (Cr), aluminium (Al) and molybdenum (Mo) in its composition, this alloy is also extensively used in many oxidizing and reducing environments [1]. The nickel-based super alloys mainly gain their high temperature strength in the austenite phase due to formation of dispersive γ' -Ni₃(Ti,Al) and γ'' -Ni₃Nb inter-metallic particles in this phase [2]. Homam Naffakh Moosavy et al. investigated the designed precipitation-strengthened nickel-based super alloys by using different welding parameters with the heat input as a constant parameter [3]. Mankins

Technical Editor: Márcio Bacci da Silva.

✉ Kanhaiya Saw
kanhaiya0555@gmail.com

Prabhat Kumar
kumar.prabhat0365@gmail.com

¹ Department of Mechanical Engineering, IIT (ISM), Dhanbad 826004, India

² Faculty of Manufacturing Technologies, Technical University of Kosice, Bayerova, Presov, Slovakia

³ Institute of Geonics AS CR, v. v. i., Olomouc, Czech Republic

Table 1 Chemical composition of base metal alloy

Element	Ni	Cr	Mo	Fe	Co	Ti	Si	Al	C	O	Cl
Weight%	50.79	21.13	9.76	1.07	10.97	0.45	0.27	1.05	3.04	1.06	0.42

et al. studied the microstructure and phase stability of this alloy. They observed the major phase emerging in the alloy after exposure to temperature in the range of 649–1039 °C [4]. This phase remained stable and precipitated as discrete particles at any temperature. Cabibbo et al. studied the microstructural modifications in the presence of the δ -phase and found a good creep response at 700 °C. This response was also compared with the result found at 800 °C of temperature [5]. The grain boundaries were observed to start displacing towards the steady-state creep region, around which the carbides dissolved. Shah Hosseini et al. investigated the microstructure and mechanical properties of Inconel 617/310 austenitic stainless steel dissimilar welds. They used three types of filler materials, Inconel 617, Inconel 82 and 310 austenitic stainless steels to obtain dissimilar joints using the gas tungsten arc welding process. The result showed that welds produced by 617 and 310 alloys as filler materials give the highest and the lowest ultimate tensile strength and total elongation, respectively [6]. Laser welding is one of the new joining technologies that have been receiving growing attention because of its exceptional features and potential. This process has a number of advantages as compared to conventional thermal joining processes. High scanning velocity, low heat affected zone, less distortion, high controllability and the ability to produce highly intensified heat source that makes highly precise welding possible [7]. Through this technique, high range of complex weld geometries and configurations can be attained with optimum level of productivity, exceptional weld quality and flexibility. Due to its high level of energy density in small spot dimensions, a narrow bead width, high precision and low panel distortions can be attained with laser welding. As compared to other available commercial lasers, fibre source laser involves low capital investment with several remarkable advantages that can improve the quality of the seam with very high potential. A good beam quality fibre source coupled with high continuous wave powers enables deep penetration welding as well as shallow conduction mode welding. As the low wave length of the beam allows absorption by almost all the metals and alloys, these lasers can be useful in various kinds of materials [8]. Yuwei Ai et al. studied the effect of various parameters, such as laser power, welding speed and defocusing on dissimilar material plates with a thickness 2 mm square butt weld configuration, by using a laser source [9]. Ahmad et al. applied a computational method to quantitatively predict

the thermal behaviour of various locations in the weld zone. Their results showed that the thermal behaviour in various locations of the weld zone was in good agreement with experimental results [10]. In the present work, it has been suggested to use fibre laser instead of Nd:YAG laser for welding of Inconel 617 1.5 mm thick alloy. The fibre laser has certain advantages over CO₂ and Nd:YAG lasers. The advantages are its superior quality, compact construction and low costs of operation and maintenance. Here, no filler metal is used, firstly, because the filler could eventually obstruct the laser beam, thereby interrupting the welding process. Subsequently, it results in defects. Secondly, the use of high-quality fibre laser for the welding of Inconel 617 1.5-mm-thick alloy is quite novel and the autogenous operation could significantly help in defect identification and its control.

The present study focuses fibre laser welding of Inconel 617 alloy of 1.5-mm-thin sheet. The detailed chemical composition of this material is presented in Table 1. The emphasis has been on the microstructure and the mechanical properties, i.e. microhardness, tensile strength, etc., of the alloy in the weld zone by varying various parameters, such as welding speed and laser power and comparing with base metal.

2 Experimental setup and procedure

A continuous wave fibre laser was used to weld the Inconel alloy 617 sheet as specified in Table 2. Nitrogen (N₂) was used as a shielding gas. The pressure of the nitrogen (N₂) gas was 3.0 bar. The schematic representation of a fibre laser setup is shown in Fig. 1. In order to obtain better laser welding quality, two welding parameters, welding power and welding speed, were varied and rest of the welding parameters were kept constant. The schematic representation of CAD model of fibre laser welding is shown in Fig. 2.

Table 2 Laser system specifications

Laser system	Maximum output power	Emission wavelength	Focal length	Focal point diameter
Fibre laser welding	400 W	1070 nm	30 mm	0.25 mm

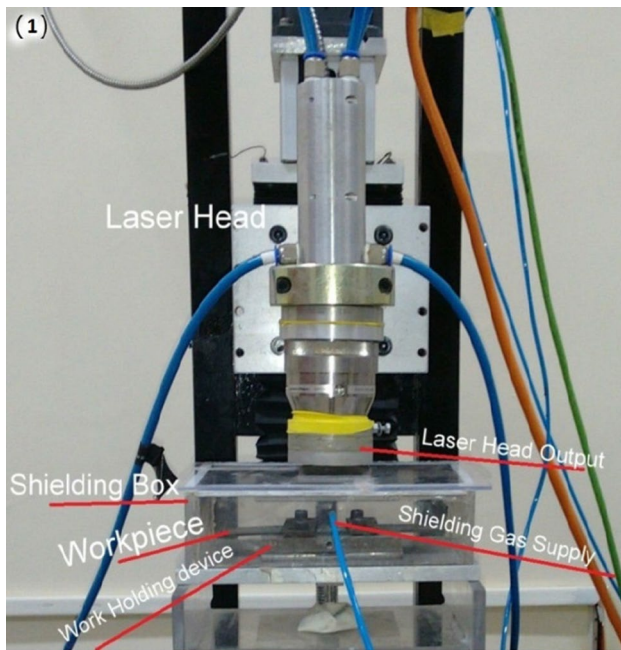


Fig. 1 Setup of fibre laser welding

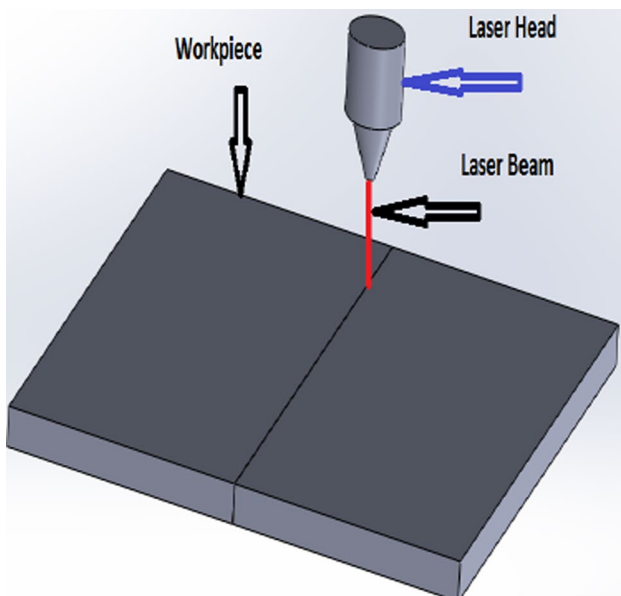


Fig. 2 CAD model of laser welding

Tables 2 and 3 present the fixed parameters and combination weld parameters used in the present study, respectively.

In the present study, the parent material, Inconel 617 of 1.5-mm-thin sheet, was used. The welding was carried out with single-pass full penetration by fibre laser welding while nitrogen was used as a shielding gas. The welding parameters, such as welding power and welding speed were varied.

Table 3 Fixed parameters used in the present study

Welding parameters	Value
Beam diameter in mm	0.25
Wave length in nm	1070
Focal position (mm)	At the surface
Gas (N ₂) pressure (bar)	3
Beam angle in degree	90
Focal length in mm	30.00

For examination of microstructure at FZ (fusion zone), HAZ (heat-affected zone) and BMZ (base metal zone), several specimens were prepared along the transverse cross-section of weldments. The specimens were prepared by grinding with 400, 600, 800, 1000, 1200 and 1500 grit of SiC paper. Grinding time for each sample was 8 min for each grit size paper. Each sample was polished at 400, 600 and 800 grit in clockwise direction and the final polishing was done at 1000, 1200 and 1600 grit size in the opposite direction of that of previous three SiC papers.

The polished surface of the samples was etched at the room temperature for 1.5 min for OM (optical microscope) and 3 min for FESEM (Supra 55, Resolution of 0.8 nm at 15 kV, and 1.6 nm at 1 kV; 12–1,000,000 \times magnification; 100 V to 30 kV acceleration voltages) observations. Glyceregia reagent (15 ml glycerol + 10 ml HCl + 5 HNO₃) was used for OM and a solution of HF + HNO₃ + distilled water was used for FESEM. Microhardness was measured at 200 μ m of welding zones, HAZ and base material at a load of 0.1 kg and for 10 s dwell time by using Vicker's microhardness tester. In the present study, the tensile test specimens were prepared as per the prescribed standard in the ASTM E-8. The tensile welds contain portions of the HAZ and the laser welding zone at the centre of the fibre laser weld, as shown in Fig. 3.

3 Results and discussion

3.1 Microstructure and XRD analysis

The images shown in Fig. 3a, b were taken with optical microscope which shows various regions of the welded sample, i.e. FZ, HAZ and BM, at a magnification of 20 \times .

The images shown in Fig. 4 were taken through FESEM in various regions of the specimen at different magnifications. Due to the full dynamic recrystallization, the microstructure consisted of fine equi-axed grains. Dendritic structure could be observed at the HAZ and FZ. Also, partially melted zone (PMZ) was seen at HAZ. On the other hand, fully melted zone (FMZ) was observed at FZ. In metallurgical term, the tree-like structure of

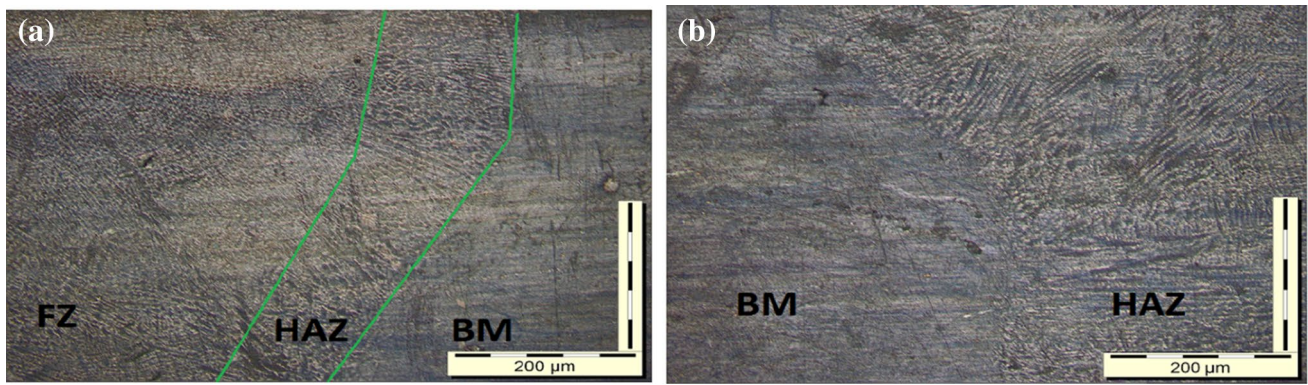


Fig. 3 a Represents various regions of welded samples, b represents BM and HAZ region

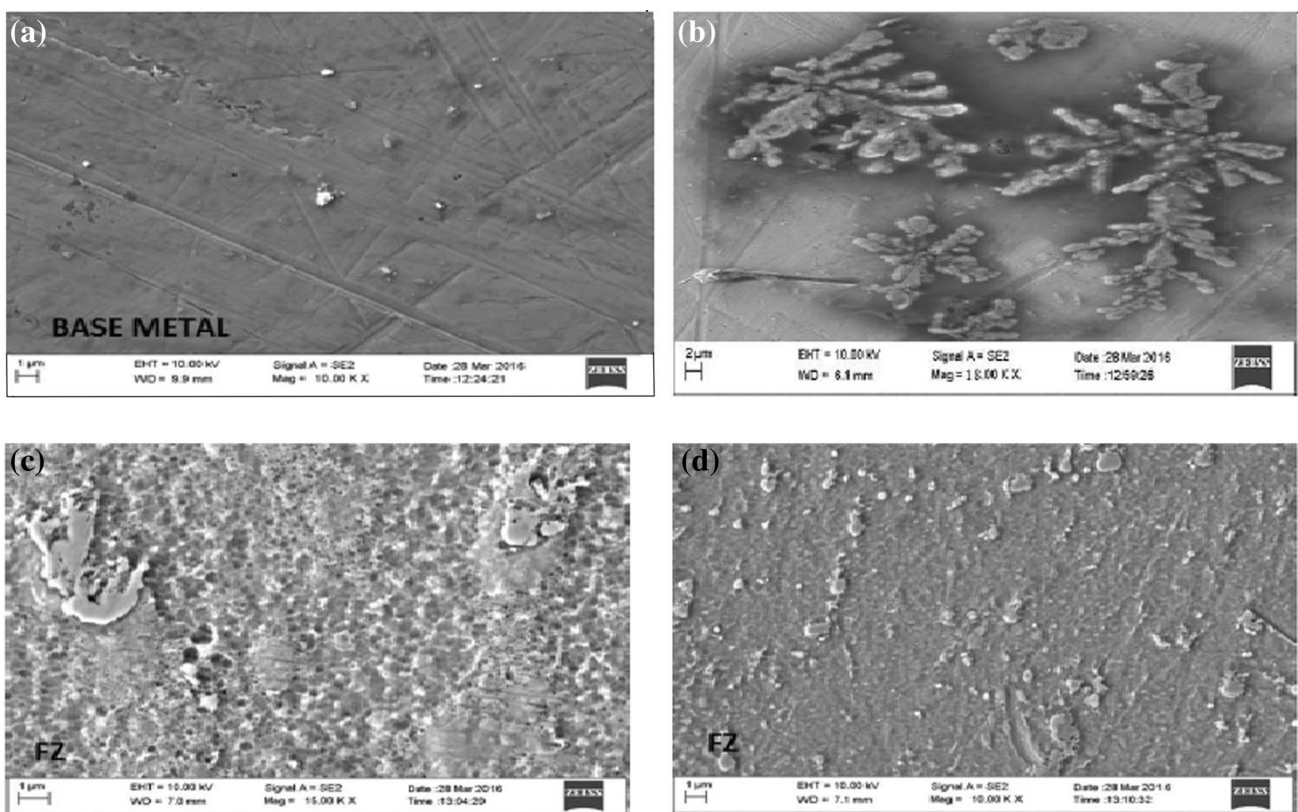


Fig. 4 a Base material, b dendrite structure, c fusion zone at 15KX, d fusion zone at 10KX

Table 4 Combination weld parameters used in the present study

Sample	Power (W)	Welding speed (mm/min)
S1	340	70
S2	320	50
S3	320	80
S4	300	90

crystal is known as dendrite structure of materials [11]. Figure 4a shows the base metal structure at 10KX, while Fig. 4b shows the dendrite growth along the direction of recrystallization at HAZ (Table 4).

The growth of dendrite structure of the sample at HAZ is due to the recrystallization of the material. When the material during welding reached its austenitic temperature

at HAZ region, the microstructure of the material tries to change. During re-solidification process, the molecules started contracting and tried to minimize its area of those surfaces having highest surface energy. Due to this contraction, the arrangement of the crystals seems like tree branches and which was observed during FESEM. In metallurgical term these tree-like structure of crystals growing as molten metal freezes are known to be dendrite structure. This growth direction may be due to anisotropic in the surface energy of solid–liquid interface. The atoms start to lose their kinetic energy as solidification proceeds. To maintain the temperature till complete solidification process, latent heat is released for the pure metal. During cooling the crystal growth takes place approximated as a parabolic needle-like crystal and grows in a shape preserving manner at constant velocity. In equi-axed solidification, the grain size mainly depends upon the nucleation and growth of the crystals. Figure 4c shows the microstructure at fusion zone. The structure in this region also has dendrite structure. But this region contains high amount of carbon due to formation of carbide at elevated temperature which can also be observed in the XRD graph. The molten metal started to accumulate in the high energy density region. The fine grain size in the fusion zone was observed and Fig. 4d shows the structural growth at the FZ (fusion zone).

The microstructure in the weld zone is expected to be changed significantly at a temperature beyond the effective liquidus temperature due to re-melting and solidification of metal in this zone.

Figure 5 shows the XRD analyses of samples which were done to understand the crystallographic structure of the specimen at various positions ($2\theta^\circ$). For the BM, the position ranged from 10° to 80° as shown in Fig. 5a in which different elements and oxides present in the alloy have been identified at the peaks. For the welded sample, the range was from 30° to 120° in which different compounds, such

as nitrides, oxides and carbides of the major elements of the alloys, were identified at the peak position as shown in Fig. 5b [12]. Hence as compared with the base metal, more complex grain structures were found in the coarse grain zone (CGZ). The analysis was done at a room temperature. The XRD graph of the BM shows the maximum percentage share of Ni and Cr elements in the alloy as observed at the position of 43.786° , 50.689° and 76.342° . At certain positions, Cr was present with the formation of its oxides.

The chromium nitrides (CrN) and nickel oxide (NiO) which are dominant compound in the FZ region as observed in Fig. 5b and the crystal structure of these compounds are face centred cubic (fcc) crystal structure along all the directions. The identical crystal structure arrangement along different direction signifies the anisotropic behaviour of the material near the FZ region. The crystal structure of other oxides and nitrides like cobalt nitride (CoN), NiMoO₄ formed in this region also found to be fcc structure of the crystals. The formation of nitride was due to the bond dissociation between the nitrogen molecules at an elevated temperature, which made it highly unstable. This nitrogen molecule was present due to the use of nitrogen as shielding gas. In the HAZ broken carbides and carbonitrides, grains were present. The fine needle-type grain structures were also found in the porosity of the HAZ. In the presence of Ni and Cr elements the solidification is always initiated with austenite dendrites. Ni, on the other hand, formed sulphate at a position 18.362° . Chromium oxide prevented further oxidation of any other element at normal condition. However, at an elevated temperature, it was not able to resist the oxidation process due to which Ni and other major elements, such as Co formed oxides during welding as very high temperatures were reached. In the CGZ, fine elongated dendritic structures were found. In case of fibre laser welding there is high cooling rate and that leads to fine dendritic structures in the CGZ.

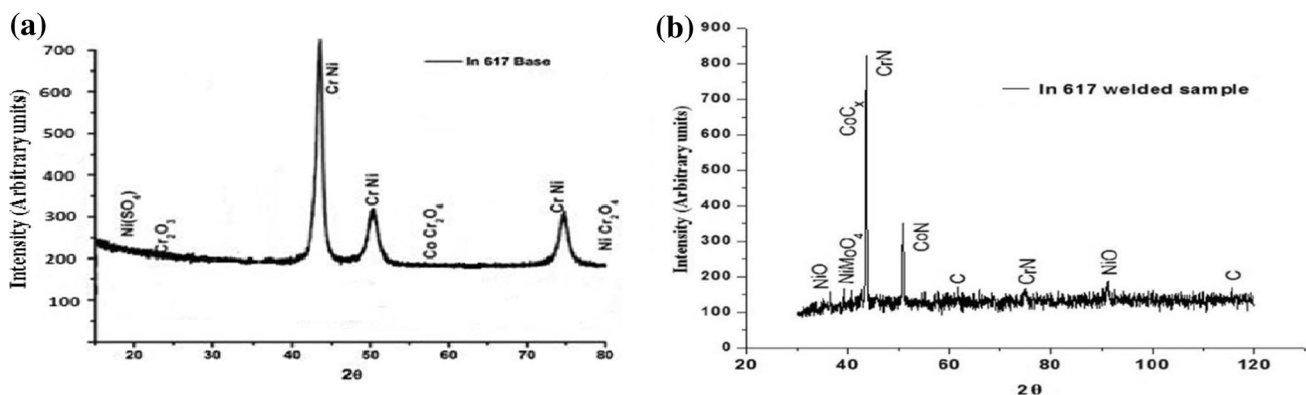


Fig. 5 a XRD graph for Inconel 617 base metal, b XRD graph for Inconel 617 at weld zone

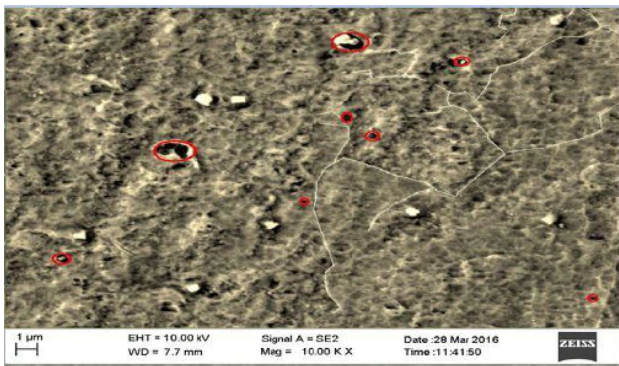


Fig. 6 FESEM image showing porosity in heat-affected zone

However, the microstructure of the FZ is much more complex due to the physical interaction between the heat source and the base metal.

Figure 6 indicates a typical morphology of porosities observed in the HAZ. It is observed that porosities appear in the vicinity of the carbides. It is also observed that the broken carbides remain inserted in the porosities (indicated by the red circle).

The energy dispersive X-ray spectroscopy (EDAX) was done at a few regions, such as at base metal and welded

region of the samples, to analyse changes in the chemical composition of the specimen before and after welding.

Figure 7a shows the chemical composition (weight%) observed in the FZ as indicated in the image. The amount of carbon in the base material (BM) was about 3.04%, which significantly increased to 5.35%. One new element that could be observed was a significant amount of nitrogen. Rest of the composition was almost the same. Hence, there was a negligible loss of alloy elements. A little amount of nitrogen was present in the FZ as shown in Fig. 7b, i.e. in weld zone that was due to use of nitrogen (N_2), as a shielding gas, is very stable at room temperature and becomes unstable at a high temperature [13].

3.2 Microhardness

The hardness distributions of the welded cross-sections were analysed with a load of 100 g using a Vicker's microhardness tester. The microhardness test was carried out at 200 μm on the surface beginning from the BM, then moving to the FZ and then coming back to the BM. The hardness was found maximum at the centre of the weld zone as compared to the BM due to its high cooling rate.

The hardness values of the fibre laser-welded FZ under different heat inputs are depicted in Fig. 8. The maximum

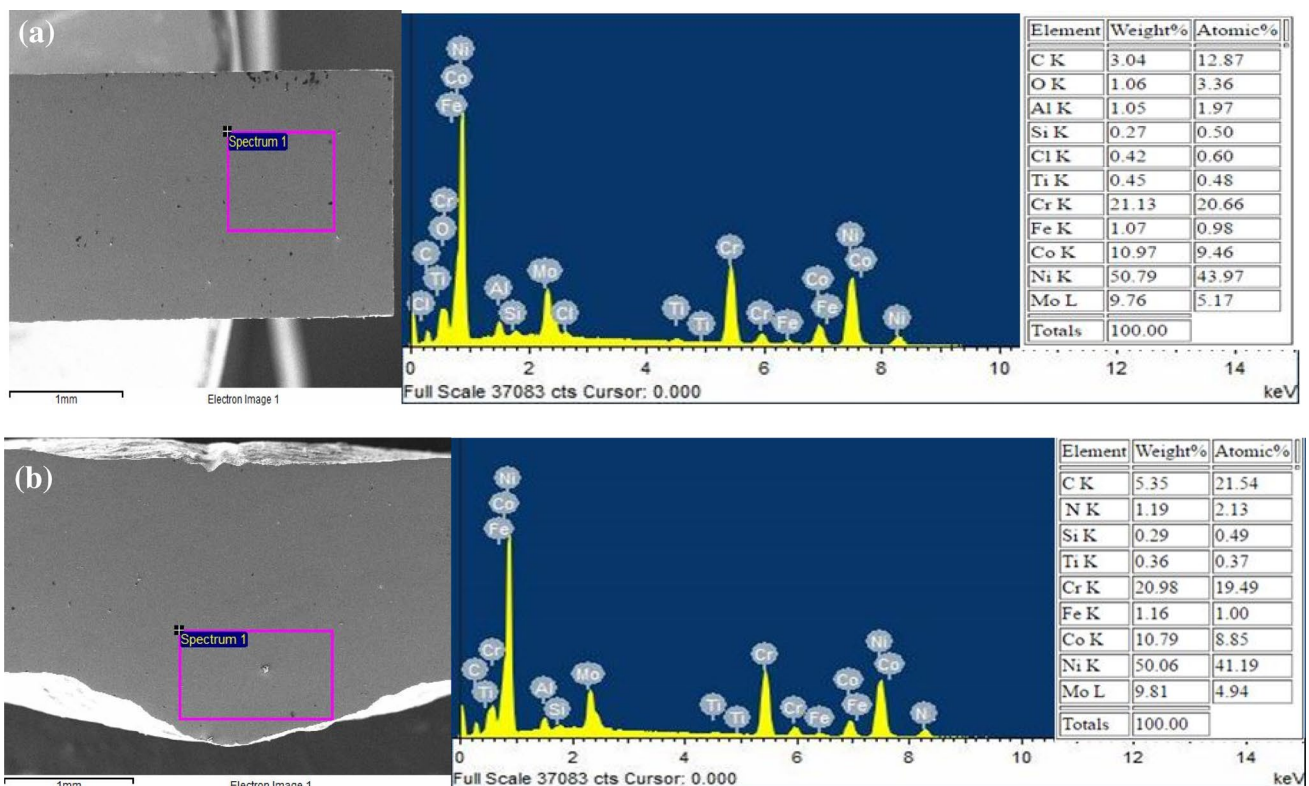


Fig. 7 a FESEM photomicrograph and EDAX spectrum of the particles marked via square area in the base metal, b FESEM photomicrograph and EDAX spectrum of the particles marked via square area

in the fusion zone of sample 4 (at welding power 300 W and welding speed 90 mm/min)

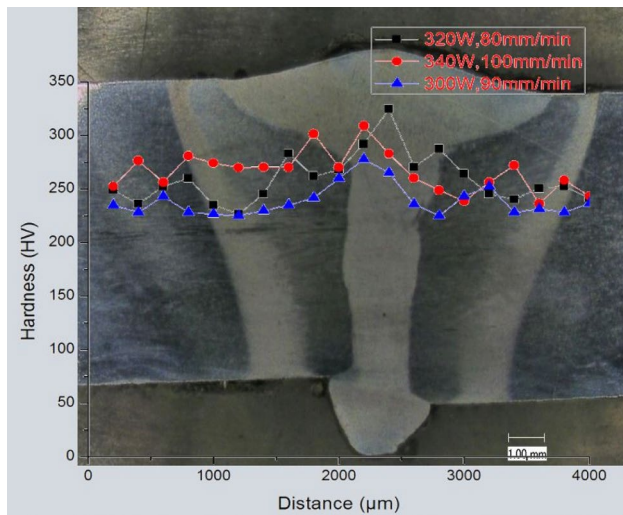


Fig. 8 Microhardness at different zones of weldments

hardness of FZ increased from 260.1 HV to 324.2 HV as the power decreased from 340 to 300 W and the difference in the hardness value was 70HV between the FZ and the BM. An increase in the welding speed from 80 mm/min to 100 mm/min only leads to a slight decrease in the hardness value. The hardness value of the weld zone varied from 258 to 312 HV and it was maximum at 80 mm/min [14]. In the HAZ, heat arises from the FZ. Therefore, the hardness in the HAZ and the base metal is lower than in the FZ and the difference is 32 HV. Figure 9 shows the average microhardness value at different zones of the weld. A study was conducted by Wenjie Ren (2015) by using fibre laser welding and CO₂ laser welding techniques on Inconel 617. The hardness value of the FZ was 259.4 and 240.1 HV, respectively [15]. The variation of hardness was observed in different regions. At the base metal region the lowest hardness value and at the fusion zone highest hardness value was observed. Various

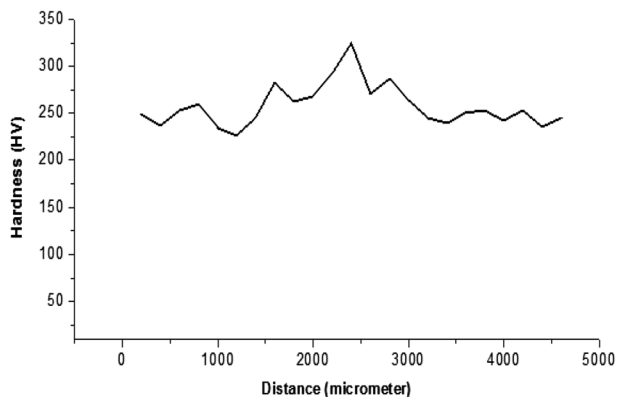


Fig. 9 Average microhardness at different zones of weld

factors influence the hardness value. The microstructure is one of the reasons because finer microstructure was observed as the microhardness value proceeds towards the fusion zone. The non-uniformity was due to variation in the concentration of different alloying elements. One more reason was the formation of carbides near and on fusion zone at elevated temperature during welding. The rapid cooling of the material after welding was another reason for the high hardness value in the fusion zone.

3.3 Tensile test

Figure 10 represents the diagram of tensile specimen having the standard dimension 160 mm × 25 mm × 1.5 mm as I-section used in the study. Figure 11a shows a standard welded tensile specimen which were cut through WEDM (wire electric discharge machining process). First, the standard tensile specimens were cut into sections of 80 mm × 25 mm × 1.5 mm and then fibre laser butt welding of the specimen was done. Tensile test was done to analyse the tensile strength and the elongation of the material. Figure 11b shows the specimen after the tensile test where they were fractured from the welded portion. A reduction of yield strength occurred in the weld due to the presence of oxide and carbide in the weld bead. However, formation of nitride was due to the bond dissociation between the nitrogen molecules at elevated temperature. The nitrogen molecule was present due to the use of nitrogen as a shielding gas. Therefore, weld failure in the FZ was observed during tensile Fig. 12.

Samples S1 and S4, which underwent higher welding speed, presented higher values of tensile strength. As a result, the weld ensured a high tensile strength, but the deformation was strongly compromised. This is due to the instability of the process and rapid cooling rate [16]. In fact, the former led to the formation of porosities, while the latter caused formation of brittle structures that had a high resistance but a low plasticity.

The surface topography in the fracture zone of the tensile specimen for the BM after the tensile test is shown in Fig. 13a, b and for the welded tensile specimen in Fig. 13c, d, respectively. The fractured surfaces of the

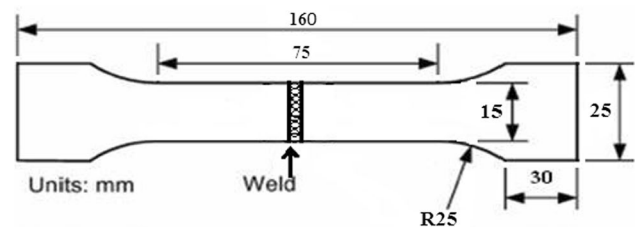


Fig. 10 Tensile specimen (thickness 1.5 mm)

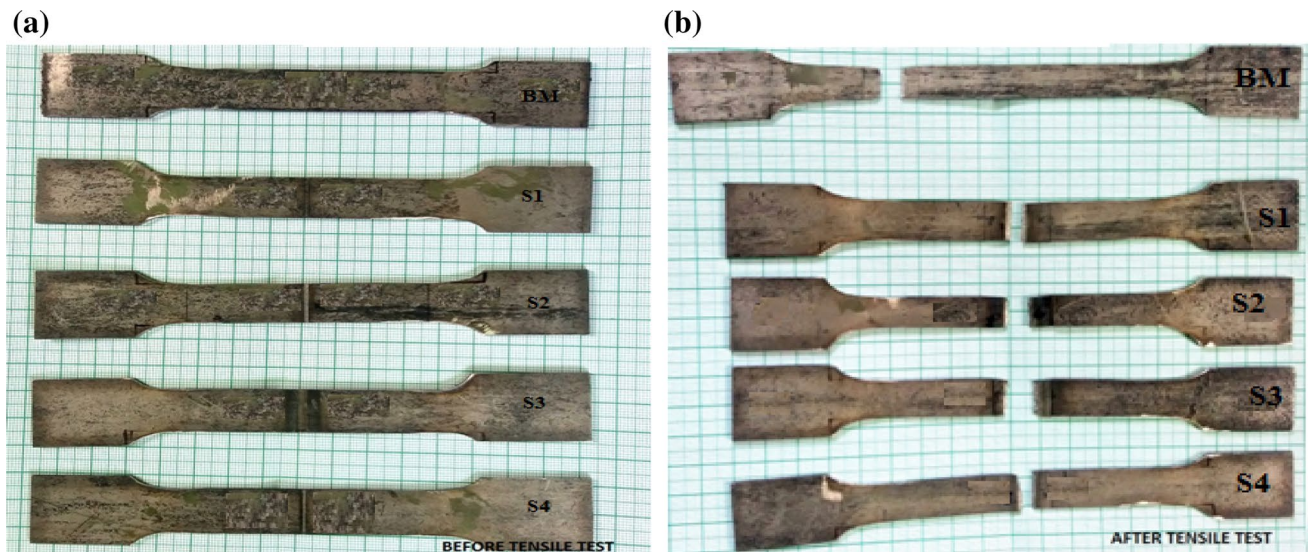


Fig. 11 **a** Tensile specimen before test, **b** tensile specimen after test

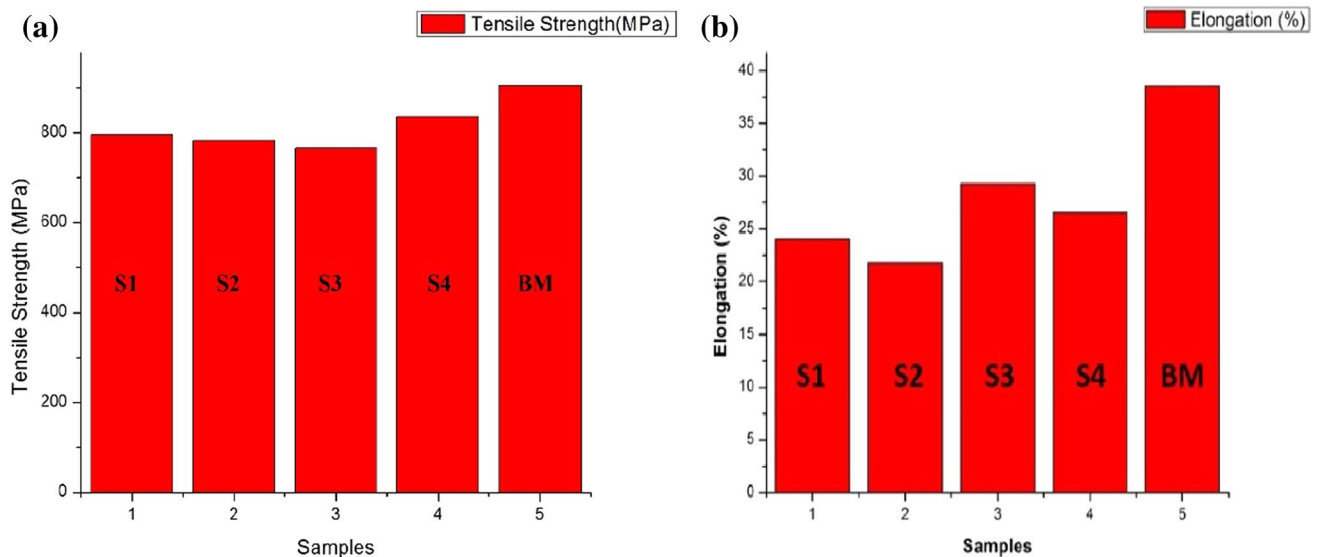


Fig. 12 **a** Represents ultimate tensile strength of samples, **b** represents percentage elongation of samples

tensile samples were analysed with FESEM. The fractured surface of the BM was found to display ductile type of fractures due to presence of dimples. The fracture of the welds occurred in the first part of the plastic field and brittle structures were formed during solidification of the weld pool. Despite the weld pool protection against contamination by atmospheric gases, a certain amount of brittle phases, such as oxides and nitrides, were formed. The fractured surface of the parent metal was found to be quite uniform with rounded edges. The crack propagation

growth direction seemed to be mostly perpendicular to the axis of the specimen. In case of the welded samples, the basic appearance was similar but a few larger dimples/voids were found. This could be due to the presence of micro-pores, detected earlier in microstructures. Micro-pores may have contributed to the reduced strength value of the welded samples.

An overall microstructural feature near the fracture region was analysed under optical microscope at a magnification of $50\times$. Figure 14a shows the microstructure

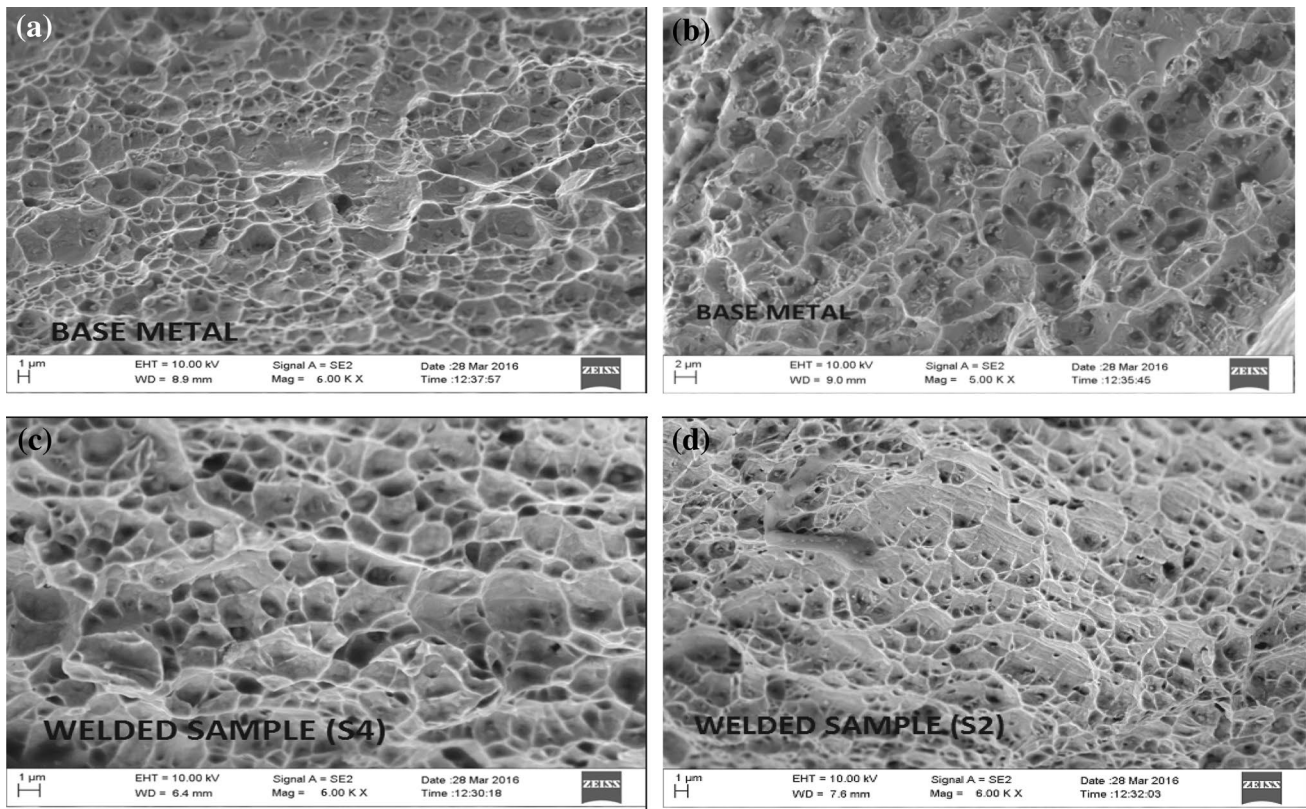


Fig. 13 **a** Fracture of base material, **b** fracture of base material, **c** fracture surface welded samples S4 (power 300 W, welding speed 90 mm/min), **d** fracture surface welded samples S2 (power 320 W, welding speed 50 mm/min)

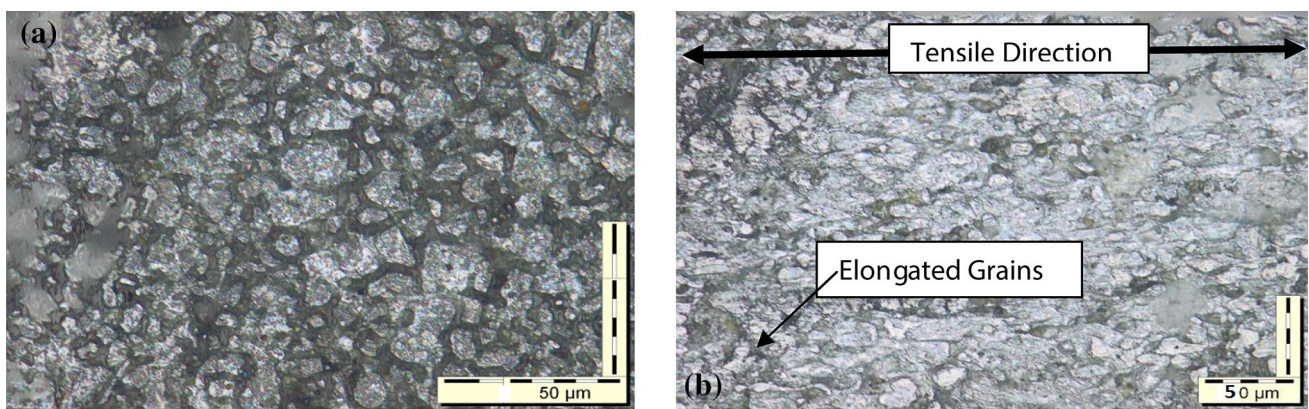


Fig. 14 **a** Top surface of tensile specimen before tensile test at 50X, **b** top surface of tensile specimen after tensile test at 50X of S1 (power 340 W, welding speed 70 (mm/min))

of the parent material in receiving condition. After the tensile test, the grains got elongated and a large number of micro-cracks developed along the direction of the applied force as can be seen in Fig. 14b. The elongated grains and micro-cracks, thus formed, could be observed in the vicinity of fracture.

4 Conclusion

The present study focused on the modern fibre laser beam welding of precipitation-strengthened nickel-base superalloy Inconel 617 by using various welding parameters. The results are summarized as follows:

- Due to rapid cooling rate in this welding process, the microhardness in the FZ is found to be higher than the microhardness in the HAZ and the BM.
- After an EDAX analysis, the carbon content was observed to have increased significantly in the weld zone and nitrogen as a new element was found because nitrogen was used as a shielding gas.
- No solidification cracks were found in the FZ. However, a few overheated points were found in the HAZ.
- The tensile strength of the specimens was found to be about 90% of that of the parent metal, while elongations of welded samples was half of that of the BM.
- Micro-pores may have contributed to the lower strength value of the welded samples.
- A reduction of yield strength was observed in the weld. As a result, weld failure in the FZ was recorded during tensile.
- In XRD analysis, the oxygen and carbon present in the metal was found to react with other major elements present in the metal. As the shielding gas used for the welding process was N₂ and the temperature during welding was very high, nitrogen easily reacted with the elements present in the metal to form nitrides.

References

1. Henderson M, Arrell D, Larsson R, Heobel M, Marchant G (2004) Nickel based superalloy welding practices for industrial gas turbine applications. *Sci Technol Weld Join* 9:13–21
2. Lippold JC, Kiser SD, DuPont JN (2011) *Welding metallurgy and weldability of nickel-base alloys*. Wiley, New Jersey
3. Moosavy HN, Aboutalebi MR, Seyedein SH, Goodarzi M, Khodabakhshi M, Mapelli C, Barella S (2014) Modern fibre laser beam welding of the newly-designed precipitation-strengthened nickel-base superalloys. *Opt Laser Technol* 57:12–20
4. Mankins WL, Hosier JC, Bassford TH (1974) Microstructure and phase stability of Inconel alloy 617. *Metall Trans* 5(12):2579–2590
5. Cabibbo M, Gariboldi E, Spigarelli S, Ripamonti D (2008) Creep behavior of INCOLOY alloy 617. *J Mater Sci* 43:2912–2921
6. Shah Hosseini H, Shamanian M, Kermapur A (2011) Characterization of microstructures and mechanical properties of Inconel 617/310 stainless steel dissimilar welds. *J Mater Charact* 62(4):425–431
7. Quintino L, Costa A, Miranda R, Yapp D (2007) Welding with high power fibre lasers—a preliminary study. *Mater Des Issue* 4:1231–1237
8. Totemeier TC, Lian H, Clark DE, Simpson JA (2005) Microstructure and strength characteristics of alloy 617 welds. *INL/EXT-05-00488*
9. Ai Yuewei, Jiang Ping, Shao Xinyu, Wang Chunming, Li Peigen, Gaoyang Mi Yang Liu, Liu Wei (2016) A defect-responsive optimization method for the fibre laser butt welding of dissimilar materials. *J Mater Des* 90:669–681
10. Ebrahimi AN, Arab NBM, Gollo MH (2016) Thermal analysis of laser beam welding of nickel-based super alloy Inconel 625 to AISI 316L, using Gaussian optics theory in keyhole. *J Braz Soc Mech Sci Eng* 38:1199–1206. doi:10.1007/s40430-015-0422-5
11. Naffakh H, Shamanian M, Ashrafzadeh F (2009) Dissimilar welding of AISI 310 austenitic stainless steel to nickel-based alloy Inconel 657. *J Mater Process Technol* 209:3628–3639
12. El-Awadi GA, Abdel-Samad S, Elshazly ES (2016) Hot corrosion behavior of Ni based Inconel 617 and Inconel 738 superalloys. *J Appl Surf Sci* 378:224–230
13. Elmer JW, Vaja J, Carlton HD, Pong R (2015) The effect of Ar and N₂ shielding gas on laser weld porosity in steel, stainless steels, and nickel. *Suppl Weld J* 94(10):313s–325s
14. Totemeier TC, Tian H, Clark DE, Simpson JA (2005) Microstructure and strength characteristics of alloy 617 welds. *INL/EXT-05-00488*
15. Ren W, Lu F, Yang R, Liu X, Li Z, Hosseini SRE (2015) A comparative study on fibre laser and CO₂ laser welding of Inconel 617. *Mater Des* 76:207–214
16. Liu Wen, Fenggui Lu, Yang Renjie, Tang Xinhua, Cui Haichao (2015) Gleeble simulation of the HAZ in Inconel 617 welding. *J Mater Process Technol* 225:221–228